

# Detection of a branched alkyl molecule in the interstellar medium: *iso*-propyl cyanide

Arnaud Belloche,<sup>1\*</sup> Robin T. Garrod,<sup>2</sup> Holger S. P. Müller,<sup>3</sup> Karl M. Menten<sup>1</sup>

<sup>1</sup>Max-Planck-Institut für Radioastronomie, Auf dem Hügel 69, 53121 Bonn, Germany

<sup>2</sup>Center for Radiophysics and Space Research, Cornell University, Ithaca, NY 14853-6801, USA

<sup>3</sup>I. Physikalisches Institut, Universität zu Köln, Zùlpicher Str. 77, 50937 Köln, Germany

\*To whom correspondence should be addressed; E-mail: belloche@mpifr-bonn.mpg.de.

**The largest non-cyclic molecules detected in the interstellar medium (ISM) are organic with a straight-chain carbon backbone. We report an interstellar detection of a branched alkyl molecule, *iso*-propyl cyanide (*i*-C<sub>3</sub>H<sub>7</sub>CN), with an abundance 0.4 times that of its straight-chain structural isomer. This detection suggests that branched carbon-chain molecules may be generally abundant in the ISM. Our astrochemical model indicates that both isomers are produced within or upon dust grain ice mantles through the addition of molecular radicals, albeit via differing reaction pathways. The production of *iso*-propyl cyanide appears to require the addition of a functional group to a non-terminal carbon in the chain. Its detection therefore bodes well for the presence in the ISM of amino acids, for which such side-chain structure is a key characteristic.**

Around 180 molecules have been detected so far in the interstellar medium (ISM) (1). Apart from the fullerenes that are cyclic, the largest of these interstellar molecules are organic with a straight-chain carbon backbone. However, more complex molecules have been identified in

meteorites found on Earth, including more than 80 amino acids (2) – the building blocks of proteins. The composition of these meteoritic amino acids suggests that they or their direct precursors have an interstellar origin (3). Chemistry at work in the ISM may thus be capable of producing organic molecules more complex than those detected so far and thus of great importance to astrobiology. However, the degree of complexity that may be reached in the ISM is still an open question, as well as how widespread these complex organic molecules are in our galaxy.

Our previous observations of the star-forming region Sagittarius B2(N) – hereafter Sgr B2(N) – yielded the first interstellar detection of the straight-chain organic molecule *normal*-propyl cyanide ( $n\text{-C}_3\text{H}_7\text{CN}$ ), the largest molecule yet detected in this source (4). This spectral line survey, conducted using the 30-m single-dish radio telescope of the Institut de Radioastronomie Millimétrique (IRAM), provided continuous spectral coverage throughout the 3-mm transmission window of Earth’s atmosphere (5). It allowed the identification of other complex organic species such as ethyl formate (4) and aminoacetonitrile (6), a possible precursor of the amino acid glycine. On the basis of the success of this single-dish line survey, we performed a survey in the same waveband by using the Atacama Large Millimeter/submillimeter Array (ALMA), resulting in an increase of more than one order of magnitude in both sensitivity and angular resolution. This interferometric project, called EMOCA (Exploring Molecular Complexity with ALMA), aims to decipher the molecular content of Sgr B2(N) in order to test the predictions of astrochemical numerical simulations and to gain insight into the chemical processes at work in the ISM.

Sgr B2 is the most massive star-forming region in our galaxy. It is located close to the Galactic Center, which is  $8.34 \pm 0.16$  kpc from the Sun (7). Sgr B2 contains two main sites of star formation, Sgr B2(N) and Sgr B2(M) that, since the early 1970s, have turned out to be the best hunting ground for complex organic molecules in the ISM. Their immense hydrogen

column densities that signify large quantities of gas enable the detection of low-abundance species. Sgr B2(N) itself contains two dense, compact, hot cores that are separated by about  $5''$  ( $\sim 40,000$  AU in projection) (6).

Propyl cyanide ( $C_3H_7CN$ , hereafter PrCN) is the smallest alkyl cyanide that exists in several distinct isomers (Fig. 1): the chain isomer *normal*- or *n*-PrCN (also known as butyronitrile or 1-cyanopropane) and the branched isomer *iso*- or *i*-PrCN (also known as *iso*-butyronitrile or 2-cyanopropane). *n*-PrCN is the smallest alkyl cyanide that exists in several distinct conformations. The CN group can be attached to the terminal C of the propyl group in the CCC plane, trans to the CCC chain, leading to the *anti* conformer, also known as *trans* (Fig. 1C); it can also be attached to the propyl group rotated by  $\pm 120^\circ$  with respect to the CCC plane, leading to the *gauche* conformer (Fig. 1B). The rotational spectrum of *i*-PrCN, previously only studied to a limited extent in the microwave region, has recently been recorded extensively in the laboratory from the microwave to the submillimeter wave region along with a redetermination of the dipole moment (8).

We used ALMA in 2012 to perform a full spectral line survey toward Sgr B2(N) in the 3 mm atmospheric window between 84 and 111 GHz (9). We identified the detected lines by modeling the molecular emission under the assumption of local thermodynamic equilibrium. By employing predictions from the Cologne Database for Molecular Spectroscopy (10), we assigned emission features to *i*-PrCN or *n*-PrCN (9). To interpret the astronomical detections, we performed numerical simulations of the chemistry occurring during the evolution of a hot core (9).

Many spectral lines are detected in the ALMA data toward both of the hot cores embedded in Sgr B2(N). These spectra are very close to the confusion limit, i.e., signal from a spectral line is detected in nearly every spectral channel. The lines are narrower toward the northern, less prominent hot core (full width at half maximum, FWHM,  $\sim 5$  km s $^{-1}$ ) than toward the

southern, more prominent one. The detection of faint lines from rare species is therefore easier toward the former and we focus on this one in the present work. We constructed a preliminary model of the emission of all molecules previously detected, on the basis of our analysis of the previous single-dish survey of Sgr B2(N) (5). In this way, the risk of mis-assigning a line to a new species is reduced. About 50 and 120 transitions of *i*-PrCN and *n*-PrCN, respectively, are detected toward the northern hot core (Fig. 2A and B and Figs. S1 and S2). On the basis of this model, we selected the least contaminated transitions and produced contour maps of their intensity integrated over their line profile (Fig. 2C and E and Figs. S3 and S4). From these maps, we derive a deconvolved angular size of  $1.0'' \pm 0.3''$  (FWHM) for the region where both species emit. We used the population diagram method (11) to estimate a rotation temperature of  $153 \pm 12$  K (SEM), which characterizes the emission of both molecules (9).

With the size and temperature derived above and a linewidth measurement of  $5 \text{ km s}^{-1}$ , we obtain a good fit to all transitions of *i*-PrCN and *n*-PrCN detected toward the northern hot core of Sgr B2(N). After correction for the contribution of vibrationally excited states (9), we derive column densities of  $7.2 \pm 1.4 \times 10^{16} \text{ cm}^{-2}$  and  $1.8 \pm 0.4 \times 10^{17} \text{ cm}^{-2}$  (SEM), respectively, which yields an abundance ratio [*i*-PrCN]/[*n*-PrCN] of  $0.40 \pm 0.06$  (SEM). The latter uncertainty assumes the same source size and rotation temperature for both isomers. With the  $\text{H}_2$  column density derived from the continuum emission (9, Fig. 2D), we deduce average abundances relative to  $\text{H}_2$  of  $1.3 \pm 0.2 \times 10^{-8}$  for *i*-PrCN and  $3.2 \pm 0.5 \times 10^{-8}$  (SEM) for *n*-PrCN. The latter uncertainties assume the same rotation and dust temperatures, and take neither possible contamination of the continuum emission by free-free emission nor uncertainties on the dust properties into account.

The recently developed chemical kinetics model MAGICKAL (Model for Astrophysical Gas and Ice Chemical Kinetics And Layering, 12) was used to simulate the time-dependent chemistry of the source. The model begins with a cold collapse phase, during which abundant

ice mantles, composed of simple H, O, C, and N-bearing molecules, are formed on dust-grain surfaces. The cold stage is followed by a warm-up stage, during which the dust and gas temperature rises from  $\sim 8$  K to 400 K. The majority of complex organic molecule formation occurs during this stage, through the addition of simple and complex radicals within and upon the ice mantles.

The model produces time-dependent chemical abundances (with respect to  $H_2$ ) for various cyanide molecules (Fig. 3). The model temperatures at which each molecule's peak abundance is attained (Table S2) may be considered representative of the excitation temperature at which most of the emission from each molecule would occur, assuming local thermodynamic equilibrium. The desorption temperature of each PrCN isomer is  $\sim 150$  K, with peak gas-phase abundances achieved at 160 K. This agrees well with the rotation temperatures that we determine from observational data for these molecules.

The majority of each of the two PrCN isomers form in or on the dust-grain ices at around 55–75 K in the model. However, the model also indicates that, whereas many similar chemical pathways are open to both *i*-PrCN and *n*-PrCN, the dominant formation route in each case is different. The greatest contribution to *i*-PrCN production comes from the reaction of CN radicals (which are accreted from the gas) with the  $CH_3CHCH_3$  radical. The latter derives from the earlier gas-phase formation of  $C_3$ , which is hydrogenated and stored on the grains as  $C_3H_2$ ,  $C_3H_4$ , and  $C_3H_6$ . The addition of atomic hydrogen to propylene ( $C_3H_6$ ) significantly favors the production of  $CH_3CHCH_3$ , whose radical site lies at the secondary carbon atom (13).

Because the production – either by hydrogen addition or abstraction processes – of radicals such as  $CH_2CH_2CH_3$  and  $CH_2CH_2CN$  (whose radical site is at the primary carbon atom) is strongly disfavored versus their equivalent *iso*- forms, we find that the dominant formation mechanism for *n*-PrCN is the addition of  $C_2H_5$  and  $CH_2CN$  – a process which has no equivalent for the production of *i*-PrCN. The radicals form through the abstraction of hydrogen by OH,

from  $C_2H_6$  and  $CH_3CN$ , respectively. *i*-PrCN production dominates all reaction mechanisms for which parallel processes are available to both isomers.

Although the overall peak gas-phase values of *i*-PrCN and *n*-PrCN produced by the models are similar, they show a slight bias toward *i*-PrCN production (2.2:1), rather than the observed bias toward *n*-PrCN (0.4:1). This may be caused by the poorly-defined rates for barrier-mediated surface reactions, such as  $H + C_3H_6 \rightarrow CH_3CHCH_3$  and  $OH + CH_3CN \rightarrow CH_2CN + H_2O$ , for which only gas-phase rates have been measured, and whose behavior may be somewhat different on an ice surface.

Amid the growing understanding that complex organic molecules could form on the surface of dust grains, the formation of branched alkyl molecules in the ISM was suggested theoretically in the 1980s (14) but no such molecules were detected until now. The detection of a branched alkyl molecule in Sgr B2, with an abundance similar to its straight-chain isomer, indicates a further divergence between the chemistry of star-forming regions like Sgr B2 and quiescent regions. These less active regions seem to produce only linear molecules – the largest one known to date being  $HC_{11}N$  (15). The detection of a branched alkyl molecule also suggests a further link between interstellar chemistry and the molecular composition of meteorites for which branched amino acids are even found to dominate over their straight-chain isomers (16). The inherent bias toward the production of secondary rather than primary radical sites on precursor radicals suggests that branched molecules may be prevalent, and indeed dominant, in star forming regions where chemistry of sufficient complexity is reached. The detection of the next member of the alkyl cyanide series, *n*-butyl cyanide ( $n-C_4H_9CN$ ), and its three branched isomers would allow the testing of this conjecture.

## References and Notes

1. See, e.g., <http://www.astro.uni-koeln.de/cdms/molecules>.

2. Elsila, J. E., Dworkin, J. P., Bernstein, M. P., Martin, M. P. & Sandford, S. A. Mechanisms of Amino Acid Formation in Interstellar Ice Analogs. *Astrophys. J.* **660**, 911–918 (2007).
3. Botta, O. & Bada, J. L. Extraterrestrial Organic Compounds in Meteorites. *Surveys in Geophysics* **23**, 411–467 (2002).
4. Belloche, A. et al. Increased complexity in interstellar chemistry: detection and chemical modeling of ethyl formate and *n*-propyl cyanide in Sagittarius B2(N). *Astron. Astrophys.* **499**, 215–232 (2009).
5. Belloche, A., Müller, H. S. P., Menten, K. M., Schilke, P. & Comito, C. Complex organic molecules in the interstellar medium: IRAM 30 m line survey of Sagittarius B2(N) and (M). *Astron. Astrophys.* **559**, A47 (2013).
6. Belloche, A., et al. Detection of amino acetonitrile in Sgr B2(N). *Astron. Astrophys.* **482**, 179–196 (2008).
7. Reid, M. J., et al. Trigonometric Parallaxes of High Mass Star Forming Regions: The Structure and Kinematics of the Milky Way. *Astrophys. J.* **783**, 130 (2014).
8. Müller, H. S. P., Coutens, A., Walters, A., Grabow, J.-U. & Schlemmer, S. Rotational spectroscopy, dipole moment and <sup>14</sup>N nuclear hyperfine structure of *iso*-propyl cyanide. *J. Mol. Spectrosc.* **267**, 100–107 (2011).
9. Additional information is available in the supplementary materials on *Science* online.
10. Müller, H. S. P., Schlöder, F., Stutzki, J. & Winnewisser, G. The Cologne Database for Molecular Spectroscopy, CDMS: a Useful Tool for Astronomers and Spectroscopists. *J. Mol. Struct.* **742**, 215–227 (2005).

11. Goldsmith, P. F. & Langer, W. D. Population Diagram Analysis of Molecular Line Emission. *Astrophys. J.* **517**, 209–225 (1999).
12. Garrod, R. T. A Three-phase Chemical Model of Hot Cores: The Formation of Glycine. *Astrophys. J.* **765**, 60 (2013).
13. Curran, H. J. Rate constant estimation for C1 to C4 alkyl and alkoxy radical decomposition. *Int. J. Chem. Kinet.* **38**, 250–275 (2006).
14. Millar, T. J., Brown, P. D., Olofsson, H. & Hjalmarsen, A. The detection of ethanol in W51M. *Astron. Astrophys.* **205**, L5–L7 (1988).
15. Bell, M. B., et al. Detection of HC11N in the Cold Dust Cloud TMC-1. *Astrophys. J.* **483**, L61–L64 (1997).
16. Cronin, J. R. & Pizzarello, S. Amino acids in meteorites. *Adv. Space Res.* **3**, 5–18 (1983).
17. Demaison, J. & Dreizler, H. Quadrupole coupling in butyronitrile. An application of microwave fourier transform spectroscopy. *Z. Naturforsch. A* **37**, 199–200 (1982).
18. Vormann, K. & Dreizler, H. Microwave-spectrum of butyronitrile – methyl internal-rotation and N-14 quadrupole coupling. *Z. Naturforsch. A* **43**, 338–344 (1988).
19. Wlodarczak, G., Martinache, L., Demaison, J., Marstokk, K.-M. & Møllendal, H. Rotational spectrum of butyronitrile: Dipole moment, centrifugal distortion constants and energy difference between conformers. *J. Mol. Spectrosc.* **127**, 178–185 (1988); Erratum: **146**, 224 (1991).
20. Traetteberg, M., Bakken, P. & Hopf, H. Structure and conformation of gaseous butyronitrile: C–H ··· $\pi$  interaction? *J. Mol. Struct.* **556**, 189–196 (2000).

21. Durig, J. R., Player, C. M., Jr., Li, Y. S., Bragin, J. & Hawley, C. W. Low-Frequency Vibrations in Molecular Solids. XVIII. Torsional Modes and Barriers to Internal Rotation of Some Isopropyl Compounds. *J. Chem. Phys.* **57**, 4544–4555 (1972).
22. Durig, J. R., Drew, B. R., Koomer, A. & Bell, S. Infrared and Raman spectra, conformational stability, *ab initio* calculations of structure and vibrational assignment of butyronitrile. *Phys. Chem. Chem. Phys.* **3**, 766–755 (2001).
23. Maret, S., Hily-Blant, P., Pety, J., Bardeau, S. & Reynier, E. Weeds: a CLASS extension for the analysis of millimeter and sub-millimeter spectral surveys. *Astron. Astrophys.* **526**, A47 (2011).
24. Pickett, H. M., et al. Submillimeter, millimeter and microwave spectral line catalog. *J. Quant. Spectrosc. Radiat. Transfer* **60**, 883–890 (1998).
25. Ossenkopf, V. & Henning, T. Dust opacities for protostellar cores. *Astron. Astrophys.* **291**, 943–959 (1994).
26. Osorio, M., Lizano, S. & D’Alessio, P. Hot Molecular Cores and the Formation of Massive Stars. *Astrophys. J.* **525**, 808–820 (1999).
27. Garrod, R. T. A new modified-rate approach for gas-grain chemical simulations. *Astron. Astrophys.* **491**, 239–251 (2008).
28. Garrod, R. T. & Pauly, T. On the Formation of CO<sub>2</sub> and Other Interstellar Ices. *Astrophys. J.* **735**, 15 (2011).
29. Mebel, A. M. & Lin, M. C. Prediction of absolute rate constants for the reactions of NH<sub>2</sub> with alkanes from *ab initio* G2M/TST calculations. *J. Phys. Chem. A* **103**, 2088–2096 (1999).

30. Hu, W-P., Rossi, I., Corchado, J. C. & Truhlar, D. G. Molecular modeling of combustion kinetics. The abstraction of primary and secondary hydrogens by hydroxyl radical. *J. Phys. Chem. A* **101**, 6911–6921 (1997).

**Acknowledgments:** We thank D. Petry and E. Humphreys at the European ALMA Regional Center (ARC), F. Gueth at the IRAM ARC node, and D. Muders at the MPIfR for their help with the reduction of the ALMA data; S. Bardeau, S. Maret, J. Pety, M. Lonjaret, and P. Hily-Blant for the new developments implemented in the Weeds software; and M. Koerber for help with preparing Fig. 1. This work made use of the NIST Chemical Kinetics Database. This work has been supported in part by the Deutsche Forschungsgemeinschaft through the collaborative research grant SFB 956 "Conditions and Impact of Star Formation", project area B3. H.S.P.M. is very grateful to the Bundesministerium für Bildung und Forschung for support through projects FKZ 500F0901 (ICC HIFI *Herschel*) and 05A11PK3 (ALMA ARC Node). R.T.G. acknowledges support from the NASA Astrophysics Theory Program through grant NNX11AC38G. This paper makes use of the following ALMA data: ADS/JAO.ALMA#2011.0.00017.S. ALMA is a partnership of ESO (representing its member states), NSF (USA), and NINS (Japan), together with NRC (Canada) and NSC and ASIAA (Taiwan), in cooperation with the Republic of Chile. The Joint ALMA Observatory is operated by ESO, AUI/NRAO, and NAOJ. The interferometric data are available in the ALMA archive at <https://almascience.eso.org/aq/>. The chemical model input files are located at [www.astro.cornell.edu/~rgarrod/resources](http://www.astro.cornell.edu/~rgarrod/resources).

### **Supplementary Materials**

[www.sciencemag.org/content/345/6204/1584/suppl/DC1](http://www.sciencemag.org/content/345/6204/1584/suppl/DC1)

Materials and Methods

Figs. S1 to S6

Tables S1 and S2

References (17–30)

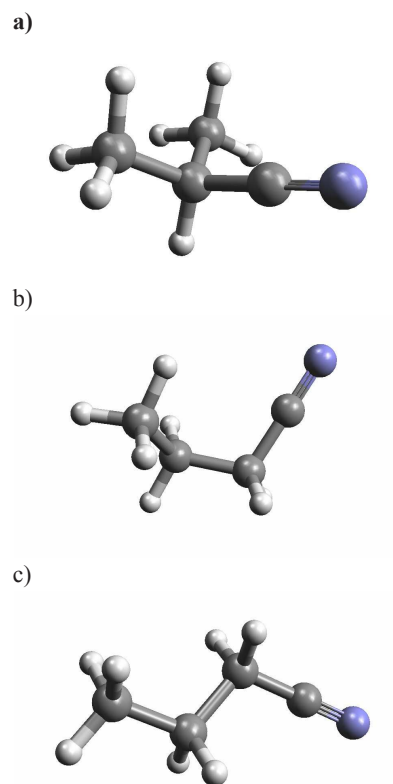


Figure 1: Models of propyl cyanide isomers and conformers. (A) *iso*-propyl cyanide ( $i\text{-C}_3\text{H}_7\text{CN}$ ). (B) *gauche-normal*-propyl cyanide ( $g\text{-}n\text{-C}_3\text{H}_7\text{CN}$ ). (C) *anti-normal*-propyl cyanide ( $a\text{-}n\text{-C}_3\text{H}_7\text{CN}$ ). C, H, and N atoms are indicated by gray, small light gray, and blue spheres, respectively.

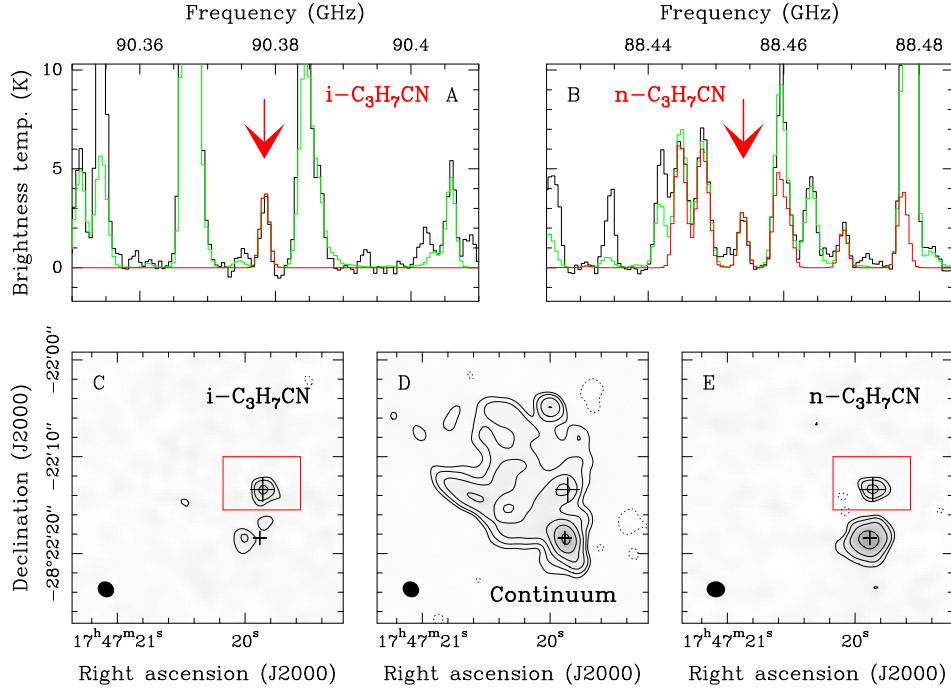


Figure 2: Examples of transitions of *i*-PrCN and *n*-PrCN toward the northern hot core of Sgr B2(N). **(A and B)** Continuum-subtracted spectrum observed with ALMA in black, the preliminary model including all identified molecules in green, and the synthetic spectra of *i*-PrCN and *n*-PrCN, respectively, in red. **(C and E)** Integrated intensity maps of the transitions of *i*-PrCN and *n*-PrCN marked with a red arrow in (A) and (B), respectively. The continuum emission at 90.5 GHz is shown in **(D)**. The negative contour (dotted blue) is  $-3\sigma$  and the positive contours (black) are  $2^i \times 3\sigma$ , with  $i$  an integer starting at 0 and  $\sigma$  the root-mean-square noise level (23 mJy beam $^{-1}$  km s $^{-1}$ , 8.3 mJy beam $^{-1}$ , and 20 mJy beam $^{-1}$  km s $^{-1}$  with half-power beam widths of  $1.8'' \times 1.6''$ ,  $1.8'' \times 1.6''$ , and  $1.9'' \times 1.6''$  in (C), (D), and (E), respectively). The large cross indicates the position of the northern hot core as traced by both molecules. The smaller cross marks the position of the main hot core that has a lower systemic velocity, which implies that the contours outside the red box do not trace the emission of *i*-PrCN and *n*-PrCN in (C) and (E), respectively. The black ellipses show the size of the respective synthetic beams.

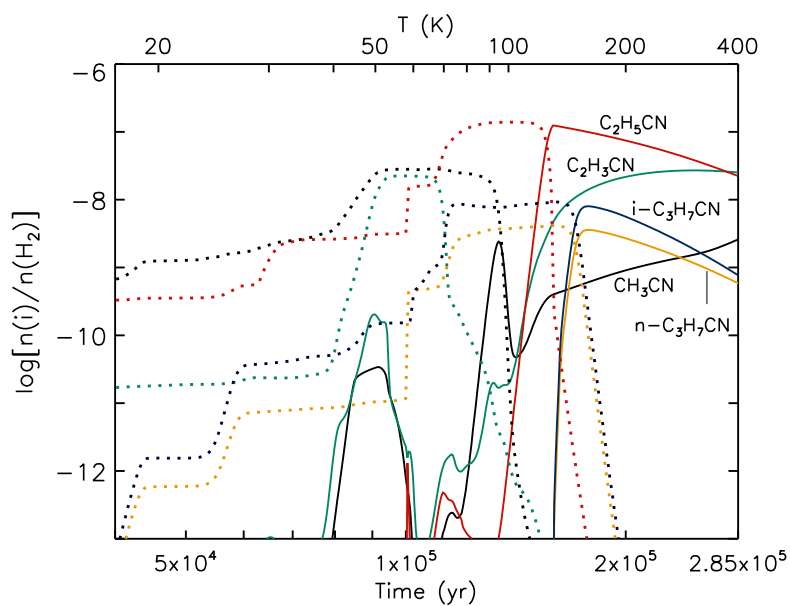


Figure 3: Simulated fractional chemical abundances of alkyl cyanides with respect to molecular hydrogen,  $H_2$ . These abundances represent the warm-up phase of hot-core evolution. Solid lines indicate gas-phase species; dotted lines of the same colour indicate the same species in the solid phase. The main phase change from solid to gas for each molecule is caused by thermal desorption from the grain surfaces, according to species-specific binding energies.

# Supplementary Materials

## Materials and Methods

**Observations.** The observations were carried out with the Atacama Large Millimeter/submillimeter Array (ALMA) between August and October 2012. The full frequency range between 84.1 and 110.7 GHz was covered with four slightly overlapping spectral setups. Each setup was observed between one and four times for a total of ten observing tracks lasting between  $\sim 0.6$  and 2 h each, but only the longest track of each setup was used in this work. The number of antennas for the selected tracks varied between 22 and 26. The size (HPBW) of the primary beam varies between  $74''$  at 84 GHz and  $56''$  at 111 GHz. The field was centered at  $\alpha_{J2000}=17^{\text{h}}47^{\text{m}}19.87^{\text{s}}$ ,  $\delta_{J2000}=-28^{\circ}22'16''$ , half way between the two hot cores embedded in Sgr B2(N) that are separated by  $4.9''$  in the north-south direction. The channel spacing was 244 kHz, but the spectra were smoothed to 488 kHz ( $1.7\text{--}1.3 \text{ km s}^{-1}$ ). Each setup consists of four spectral windows of 1875 MHz each, two per sideband. The separation between the centers of the lower and upper sidebands is 12 GHz.

**Data reduction.** The data were calibrated and imaged with CASA (Version 4.2.0, r28322). The bandpass calibration was carried out on the quasar B1730-130. The absolute flux density scale was derived from Neptune (except for the selected track of the second setup that used Titan). The phase and amplitude calibrations were performed on the quasar J1700-261. The track of the third setup was affected by an astrometry problem with Sgr B2(N) being shifted by  $(\Delta\alpha, \Delta\delta) \sim (0.5'', 0.2'')$  with respect to the other setups. This shift may be due to an inaccurate calibration of the atmospheric phase fluctuations due to the low elevation of the phase calibrator during the observations of this particular track. The offset was approximately compensated for by modifying the visibilities of the phase calibrator with the CASA task *fixvis* before the phase

calibration. After this correction, the relative positional accuracy of the four tracks used in this work is on the order of  $\pm 0.1''$  in both right ascension and declination. Three or four iterations of self-calibration were performed using a strong spectral line detected toward Sgr B2(N) in each setup. The images were produced with the CLEAN deconvolution algorithm in CASA. The size (HPBW) of the synthesized beam depends on the setup and the sideband but is typically  $2.0'' \times 1.4''$  (minimum  $1.6'' \times 1.2''$ , maximum  $3.0'' \times 1.4''$ ). The median rms noise level reached for each selected track varies between 4.4 and 9.9 mJy/beam. Based on the redundancies of the tracks and the spectral overlap between the setups, we estimate the absolute calibration uncertainty on the flux density to be on the order of 15%.

The spectra toward and around the two hot cores embedded in Sgr B2(N) are full of lines and close to the confusion limit. It is thus difficult to separate the line emission from the continuum emission in a systematic way for the full data cubes, but it is a necessary step to produce separate line and continuum maps. For each spectral window of each setup, we selected six groups of few channels that seemed to be free of strong line emission. A first-order baseline was fitted to these selected channels and the result of the fit was used to split each data cube into two cubes, one for the line emission and one for the continuum emission. Given the difference in systemic velocity between the two hot cores ( $\sim 10 \text{ km s}^{-1}$ , see 5), we selected different sets of channels for the northern and southern parts of the field.

**Laboratory spectroscopy.** Predictions of the rotational spectra of *i*-PrCN and *n*-PrCN were taken from the CDMS (10), version 1 and 2, respectively. The predictions of *i*-PrCN were based on spectroscopic parameters derived from microwave to submillimeter wave measurements (8). The dipole moment components were also redetermined in that work. Belloche et al. (4) derived spectroscopic parameters of both *gauche* and *anti* conformers of *n*-PrCN by combining data from two microwave studies (17, 18) with millimeter and submillimeter data from Wlodarczak

et al. (19).

Wlodarczak et al. (19) also determined the *a*- and *b*-dipole moment components for both conformers of *n*-PrCN and determined the *anti* conformer to be lower in energy than the *gauche* conformer by  $1.1 \pm 0.3$  kJ/mol, in contrast to an electron diffraction study (20) and to a more recent and much more accurate determination by low-temperature infrared measurements that determined the *gauche* conformer to be lower in energy by  $0.48 \pm 0.04$  kJ/mol (22). The results of our ALMA observations are fully consistent with the latter energy difference. The reverse energy ordering in the millimeter wave study (19) may, at least in part, be due to an underestimation of the strong *a*-dipole moment component of the *anti* conformer. In fact, quantum-chemical calculations on *i*-PrCN, *a-n*-PrCN and *cyclo*-PrCN (8) suggest that the *a*-dipole moment component of *a-n*-PrCN is around 4.0 D instead of the measured  $3.597 \pm 0.059$  D (19). This underestimation leads to an overestimation of the amount of *a-n*-PrCN by about one fourth because the intensity of a transition scales with the square of the dipole moment component. The experimental value of the weaker *b*-dipole moment component of almost 1.0 D may be correct, but could also be slightly underestimated. Similar quantum-chemical calculations on the dipole moment components of *g-n*-PrCN by one of us (HSPM) provide good agreement with the experiment for the *a*- and *b*-components and suggest that neglecting the small *c*-component of  $\sim 0.45$  D leads to only small errors. Nevertheless, this component was used in the second version of the *n*-PrCN CDMS entry.

A considerable part of such complex molecules resides in excited vibrational states at the elevated temperatures determined for the propyl cyanides. In particular, low-lying vibrational states are of importance. We use data from Durig et al. (21) for *i*-PrCN and from Durig et al. (22) for *n*-PrCN. Contributions from vibrationally excited states increase the partition function values at 150 K by factors of 1.64, 2.09, and 2.36 for *i*-PrCN, *g-n*-PrCN, and *a-n*-PrCN, respectively.

**Line identification and spectral modeling.** The line identification in the ALMA spectra was performed following the same strategy as for our previous, single-dish, spectral-line survey of Sgr B2(N) with the IRAM 30 m telescope (5). The main difference is that we used Weeds (23) (version of April 2014) which is part of the CLASS software (see <http://www.iram.fr/IRAMFR/GILDAS>). We built our own Weeds database containing mostly JPL (24) and CDMS (10) entries, plus a number of private entries as in Belloche et al. (5). For this work, we focused on the northern hot core embedded in Sgr B2(N) (position P2 in ref. 6). The emission of each molecule across the full 3 mm atmospheric window is modeled assuming local thermodynamic equilibrium (LTE, which means that the excitation temperature of the transitions is equal to the rotational temperature of the molecule and the kinetic temperature of the gas) with five parameters: column density, temperature, source size, velocity offset, and linewidth. We model each spectral window of each observed setup separately to account for the varying angular resolution.

A preliminary model fitting the emission detected with ALMA was constructed based on the parameters derived for all molecules identified in our single-dish survey of Sgr B2(N). This model has not been fully optimized for ALMA yet but it is already sufficiently reliable to allow for detecting new molecules in the ALMA spectra. Figures S1 and S2 show the transitions of *i*-PrCN and *n*-PrCN, respectively, identified in the ALMA spectrum of the northern hot core. Only the transitions that are not severely blended with transitions of other species are shown in these figures. Integrated intensity maps were computed for the transitions that are well fitted by our LTE model in these figures, i.e. the transitions that do not suffer from blends with identified or unidentified species. These maps are shown in Figs. S3 and S4. We stress the fact that the emission was integrated over only a few channels (typically  $\sim 11 \text{ km s}^{-1}$ ) covering each transition detected toward the northern hot core (FWHM  $\sim 5 \text{ km s}^{-1}$ ). This means that, in these figures, the contours around the main hot core, which has a systemic velocity lower by  $\sim 10 \text{ km s}^{-1}$  compared to the northern hot core (5), mainly trace other species than *i*-PrCN or

*n*-PrCN. The emission toward the northern hot core was fitted with an elliptical Gaussian for each map. The results are similar for both molecules. Ignoring the transitions from the third setup that has the largest beam and for which the absolute astrometry was readjusted, we derive equatorial offsets  $(\Delta\alpha, \Delta\delta)_{J2000} = (-0.1'' \pm 0.1'', 2.6'' \pm 0.1'')$  for the peak position with respect to the phase center and a size of  $1.0'' \pm 0.3''$  (FWHM).

Finally, we constructed population diagrams (11) for *i*-PrCN and *n*-PrCN using the transitions that are not too severely blended with emission from other identified species. Figures S5A and S6A show the population diagrams derived using the observed integrated intensities of *i*-PrCN and *n*-PrCN, respectively. Figures S5B and S6B show the same after subtracting the (model) contribution of all contaminating molecules that are included in our full LTE synthetic spectrum, like we did for our previous single-dish detection of *n*-PrCN (4). In each panel, the LTE model of *i*-PrCN or *n*-PrCN is shown in red. The observed data points that remain well above the synthetic data points in Figs. S5B and S6B are most likely contaminated by emission from still unidentified species. Nevertheless, a linear fit to these data points can give a rough estimate of the rotation temperature characterizing the emission of the molecules, provided the transitions are optically thin (which is verified to be true a posteriori). In such a diagram, the slope of the linear fit is inversely proportional to the rotation temperature. We derive  $T_{\text{ex}} = 154 \pm 99$  K for *i*-PrCN and  $153 \pm 12$  K (SEM) for *n*-PrCN. The larger uncertainty for the former is due to the narrower energy range of its detected transitions. We estimate the statistical error on the derived column densities to be on the order of 20% (SEM), with 10% coming from the uncertainty on the (*n*-PrCN) rotation temperature. This uncertainty does not take into account the uncertainty on the source size and the overall calibration uncertainty that should however both affect the column densities of *i*-PrCN and *n*-PrCN in the same way.

**Continuum emission.** The peak flux density measured toward the northern hot core at 98.8 GHz is 0.24 Jy/ $1.8'' \times 1.3''$ -beam. Assuming a dust mass opacity of  $0.01 \text{ cm}^2 \text{ g}^{-1}$  at 230 GHz (25), a dust emissivity index  $\beta = 1.0$ , a mean molecular weight per  $\text{H}_2$  molecule of 2.8, a temperature of 150 K, and that all the continuum flux is due to thermal dust emission, we derive a peak  $\text{H}_2$  column density,  $N_{\text{H}_2}$ , of  $4.2 \times 10^{24} \text{ cm}^{-2}$ . For a distance of 8.34 kpc, the measured peak flux density corresponds to a mass,  $M$ , of  $415 M_\odot$  for a region of size 12900 AU (FWHM). Assuming spherical symmetry, this translates into a mean free-particle density,  $n$ , of  $5.5 \times 10^7 \text{ cm}^{-3}$ , or a mean hydrogen density  $n_{\text{H}}$  of  $9.3 \times 10^7 \text{ cm}^{-3}$ . We extrapolate these results for the more compact region where the PrCN emission comes from (FWHM  $\sim 1.0''$ ) by assuming spherical symmetry and a density profile proportional to  $r^{-1.5}$  (26). We obtain  $N_{\text{H}_2}(1'') = 5.2 \times 10^{24} \text{ cm}^{-2}$ ,  $M(1'') = 215 M_\odot$ ,  $n(1'') = 1.1 \times 10^8 \text{ cm}^{-3}$ , and  $n_{\text{H}}(1'') = 1.8 \times 10^8 \text{ cm}^{-3}$ . Doing the same for all spectral windows of all setups, we derive the following average values and standard deviations (rms):  $N_{\text{H}_2}(1'') = 5.6 \pm 0.4 \times 10^{24} \text{ cm}^{-2}$ ,  $M(1'') = 232 \pm 17 M_\odot$ ,  $n(1'') = 1.06 \pm 0.08 \times 10^8 \text{ cm}^{-3}$ , and  $n_{\text{H}}(1'') = 1.9 \pm 0.1 \times 10^8 \text{ cm}^{-3}$ . The uncertainties are only statistical and do neither take into account the uncertainties due to the assumptions about the geometry and  $\beta$ , nor possible contamination by free-free emission.

**Astrochemical numerical simulations.** The chemical model solves the fully-coupled time-dependent chemical kinetics of nearly 700 unique chemical species, and traces their populations in the gas phase, on dust-grain/ice surfaces, and within the bulk ice mantles, during the collapse and warm-up of the hot core, as described by Garrod (12). The chemical network consists of a full gas-phase chemistry that includes ion-molecule and neutral-neutral reactions, as well as solid-phase atomic- and radical-addition reactions and photodissociation processes. The gas and grain chemical phases are coupled through gas-phase accretion and both thermal and non-thermal desorption mechanisms. The chemical kinetics are solved using the modified rate-

equation approach (27), with a standard ODE solver.

The behavior of the chemical system is determined by the physical conditions during the two modeled stages of physical evolution of the hot core. The first is a free-fall collapse from a total hydrogen density,  $n_{\text{H}}$ , of 3000 to  $2 \times 10^8 \text{ cm}^{-3}$ . The final density is consistent with the density derived for the region in the northern hot core of Sgr B2(N) from which the PrCN emission originates (see above). Gas temperatures are fixed at 10 K, while dust temperatures fall from  $\sim 18$  to 8 K, according to the visual extinction,  $A_V$ , as described by Garrod & Pauly (28). Dust-grain ice mantles form during this stage, through hydrogenation of atoms and simple molecules derived from the gas phase. The second stage consists of a physically-static warm up of both the gas and the dust, to 400 K, assuming the intermediate warm-up period of Garrod (12). The majority of complex organic chemistry occurring on the dust grains takes place during the warm-up stage, during which the mobility of reactive radicals is increased. As temperatures rise, surface molecules thermally desorb from the grain/ice surface into the gas phase, wherein the most complex molecules are typically destroyed by ion-molecule reactions.

The major elemental abundances at the beginning of the collapse stage with respect to total hydrogen are 0.09 for He,  $1.4 \times 10^{-4}$  for C,  $7.5 \times 10^{-5}$  for N, and  $3.2 \times 10^{-4}$  for O. Ice mantle molecular abundances at the end of the collapse phase, with respect to water, are 56% for CO, 18% for CO<sub>2</sub>, 7.0% for CH<sub>3</sub>OH, 2.0% for CH<sub>4</sub>, and 18% for NH<sub>3</sub>.

During the warm-up stage, reactive radicals on the dust grains can form through photodissociation of stable molecules, by H-atom abstraction by other radicals such as OH, or by H-atom addition to unsaturated molecules. Rates are determined as described by Garrod (12). Belloche et al. (4) incorporated formation and destruction mechanisms for *n*-PrCN. The new chemical model introduces a range of mechanisms for its structural isomer, *i*-PrCN. This is the first time that side-chain chemistry has been included in interstellar chemical networks.

Table S1 shows the main reactions included in the model that lead to the formation of *n*-

PrCN and *i*-PrCN upon/within the dust-grain ices. They are all assumed to proceed without a barrier. Only the final step is shown for each mechanism. The production of the larger precursor radicals involved in the listed reactions can occur through hydrogen abstraction from a saturated molecule, e.g. C<sub>3</sub>H<sub>8</sub> (either by OH or NH<sub>2</sub>). Photolysis may also produce such radicals, although other product branches are also included in the model for each photolysis event. A set of analogous reactions to some of those shown in Table S1 is also included, which consist of the addition of CH<sub>2</sub> (rather than CH<sub>3</sub>) to a radical. PrCN is then formed by the addition of a hydrogen atom. The CH<sub>2</sub> mechanisms are of only minor influence to the results. CH<sub>3</sub> can be formed by dissociation of molecules such as methanol (CH<sub>3</sub>OH), while CN also has multiple gas-phase and dust-grain routes to its formation. Some reactions between stable molecules and radicals other than OH and NH<sub>2</sub> are included in the chemical network, but these are relatively inefficient, due to significant activation energies, and at interstellar temperatures would strongly favor the abstraction of atomic hydrogen, rather than producing more complex molecular structures.

Measured gas-phase rates indicate that hydrogenation of C<sub>3</sub>H<sub>6</sub> and H-atom abstraction from C<sub>3</sub>H<sub>8</sub> preferentially result in an unpaired electron at the secondary carbon site (13, 29, 30), due to the lower activation energy, which favors *i*-PrCN production over *n*-PrCN. Hydrogenation and abstraction processes involving C<sub>2</sub>H<sub>3</sub>CN and C<sub>2</sub>H<sub>5</sub>CN, respectively, are treated similarly. Photodissociation rates are also assumed with a bias of 10:1 in favor of a radical site at the secondary carbon, although the importance of photodissociation is small compared to the former processes. All other rates and binding energies are assumed to be identical between the *i*-PrCN and *n*-PrCN forms. Binding energies of molecules for which experimental data on appropriate ice surfaces do not exist, including PrCN, are determined by interpolation of known energies for similar species or functional groups.

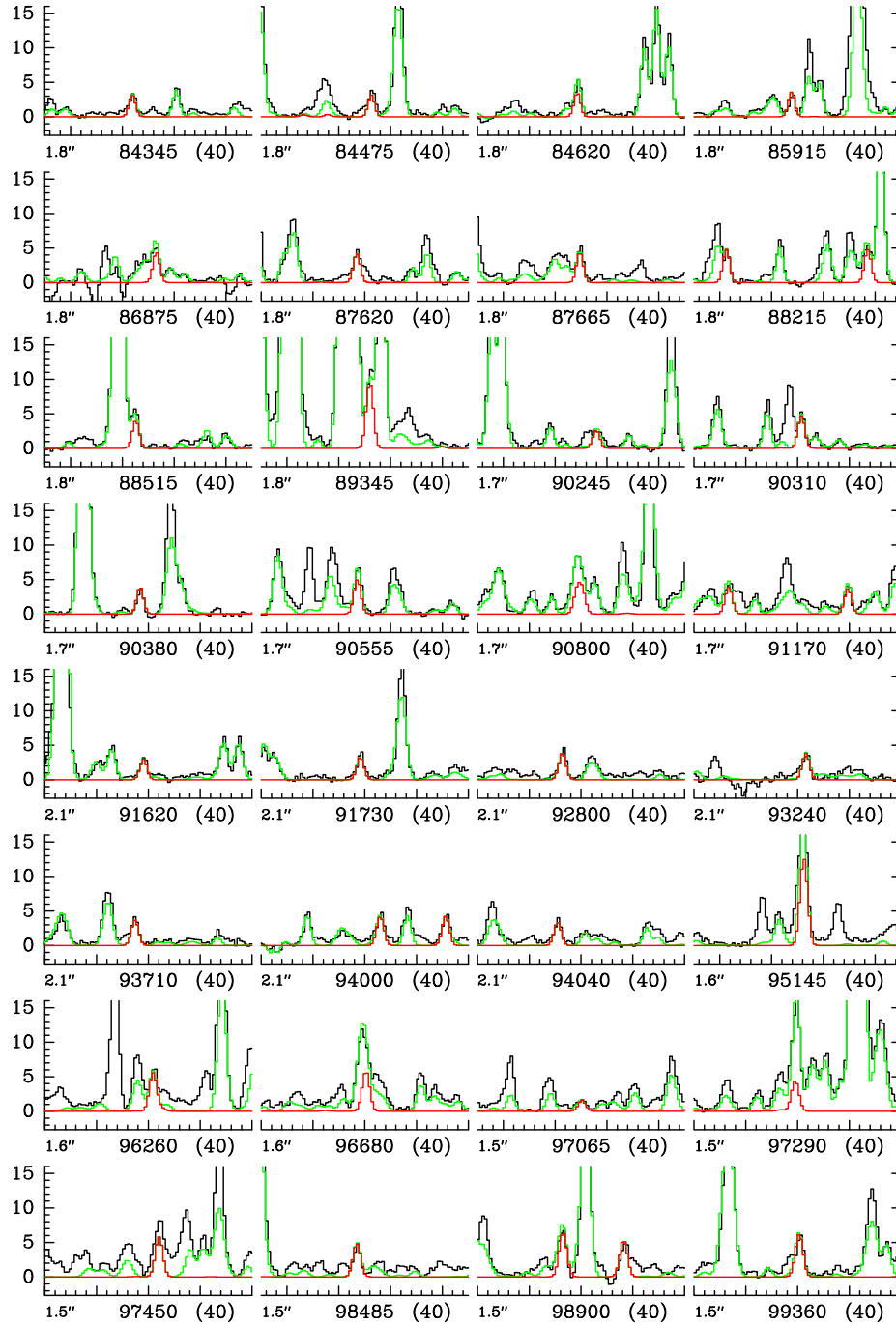


Figure S1: Transitions of *i*-PrCN detected with ALMA toward the northern hot core embedded in Sgr B2(N). The continuum-subtracted observed spectrum is shown in black, the synthetic spectrum of *i*-PrCN in red, and the preliminary model including all detected molecules in green. The x-axis of each panel is labeled with its central frequency and its frequency range in parentheses, both in MHz. The angular resolution (mean FWHM of the synthesized beam) is also indicated below each panel. The y-axis indicates the brightness temperature in K.

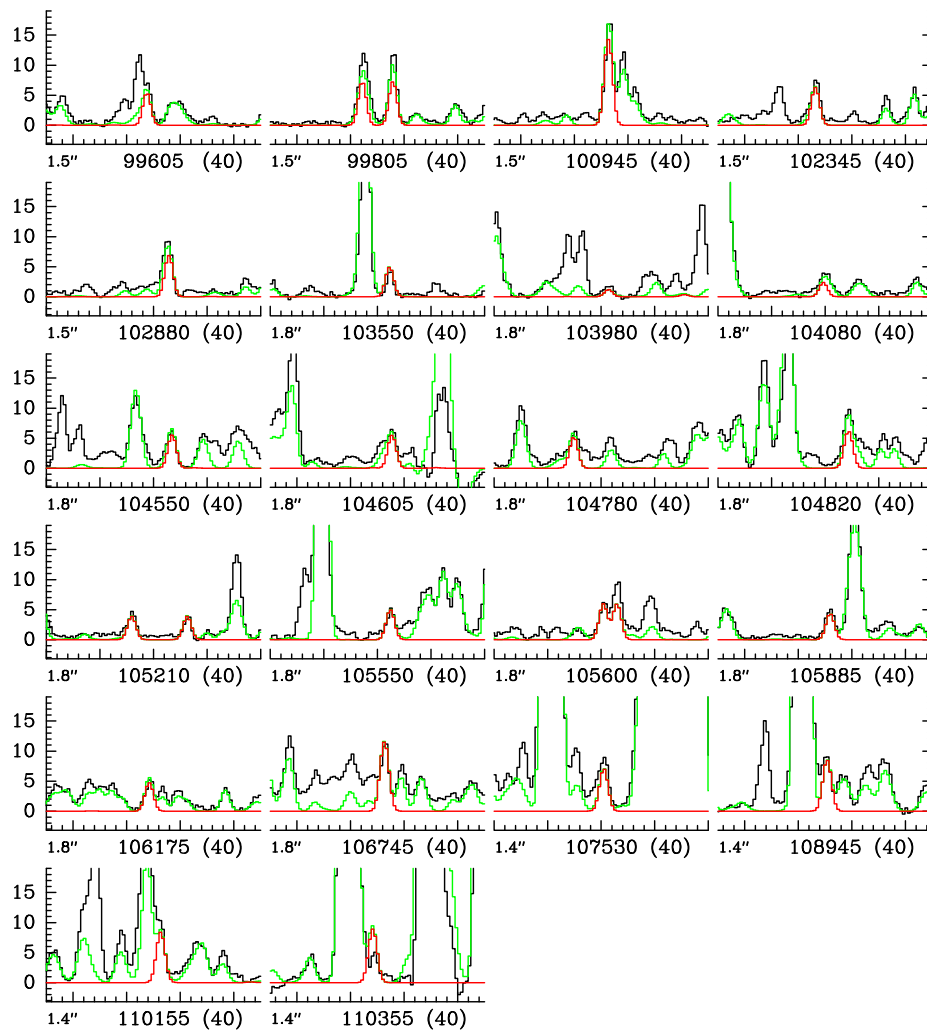


Figure S1: continued.

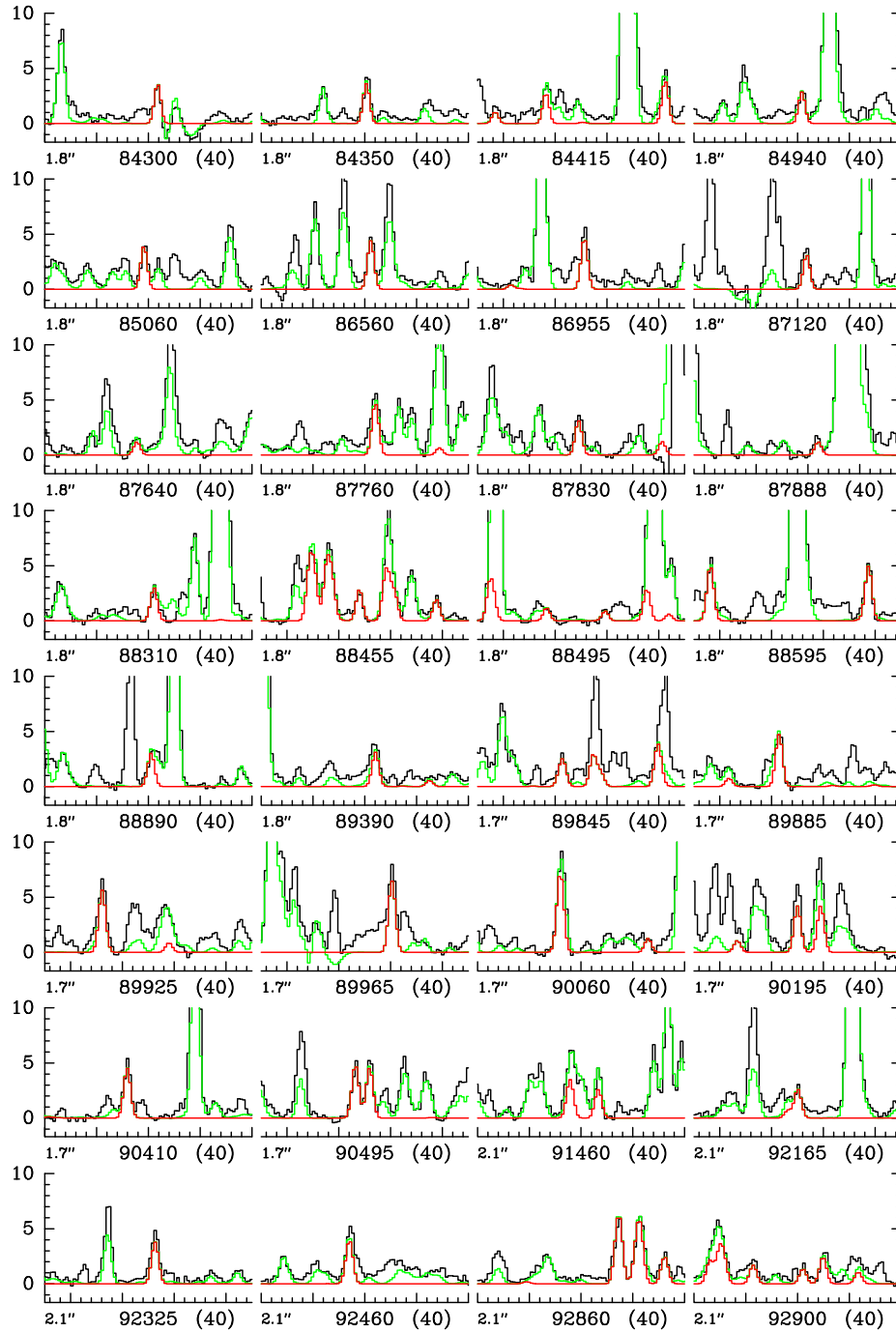


Figure S2: Transitions of  $n$ -PrCN detected with ALMA toward the northern hot core embedded in Sgr B2(N). See caption of Fig. S1 for more details.

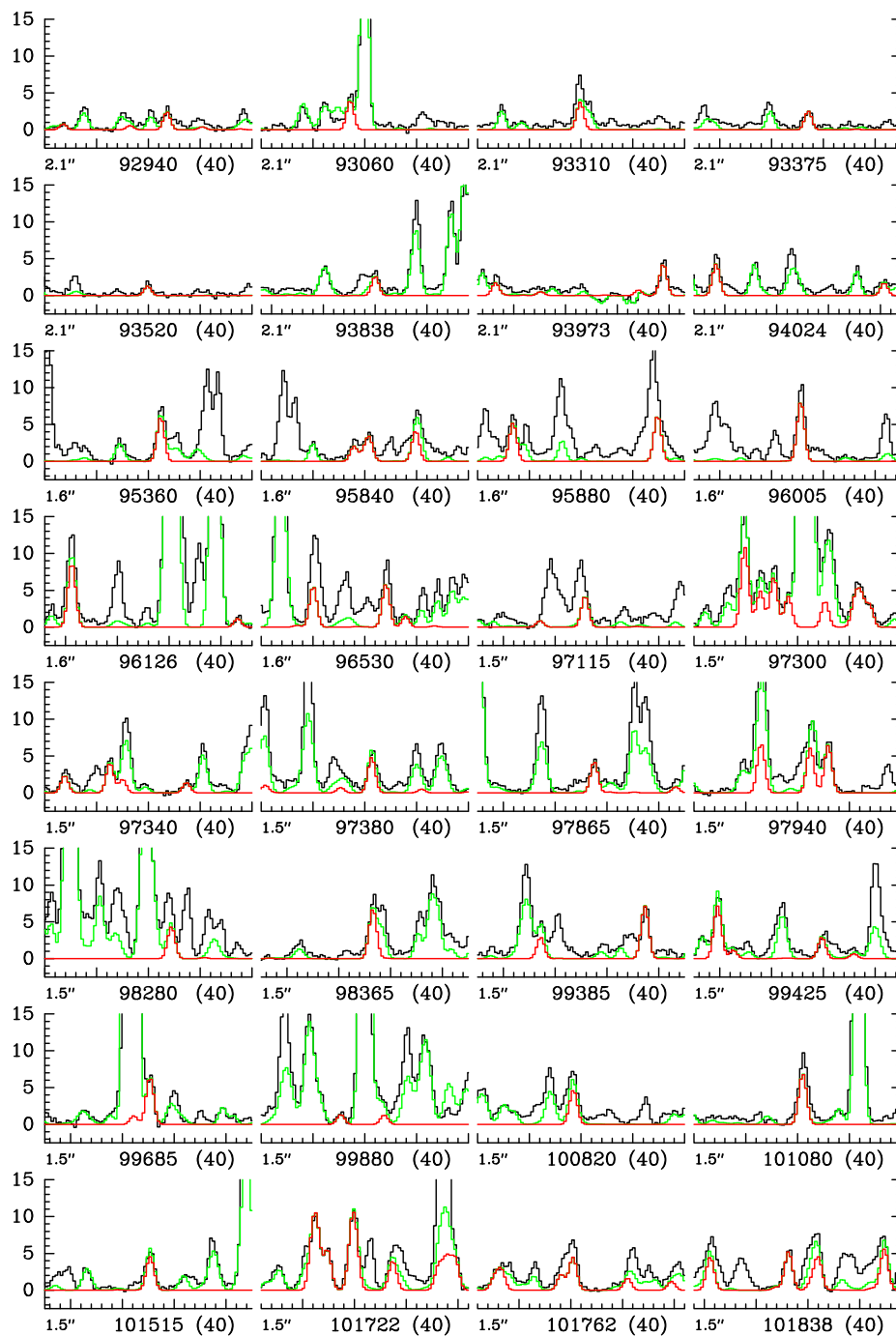


Figure S2: continued.

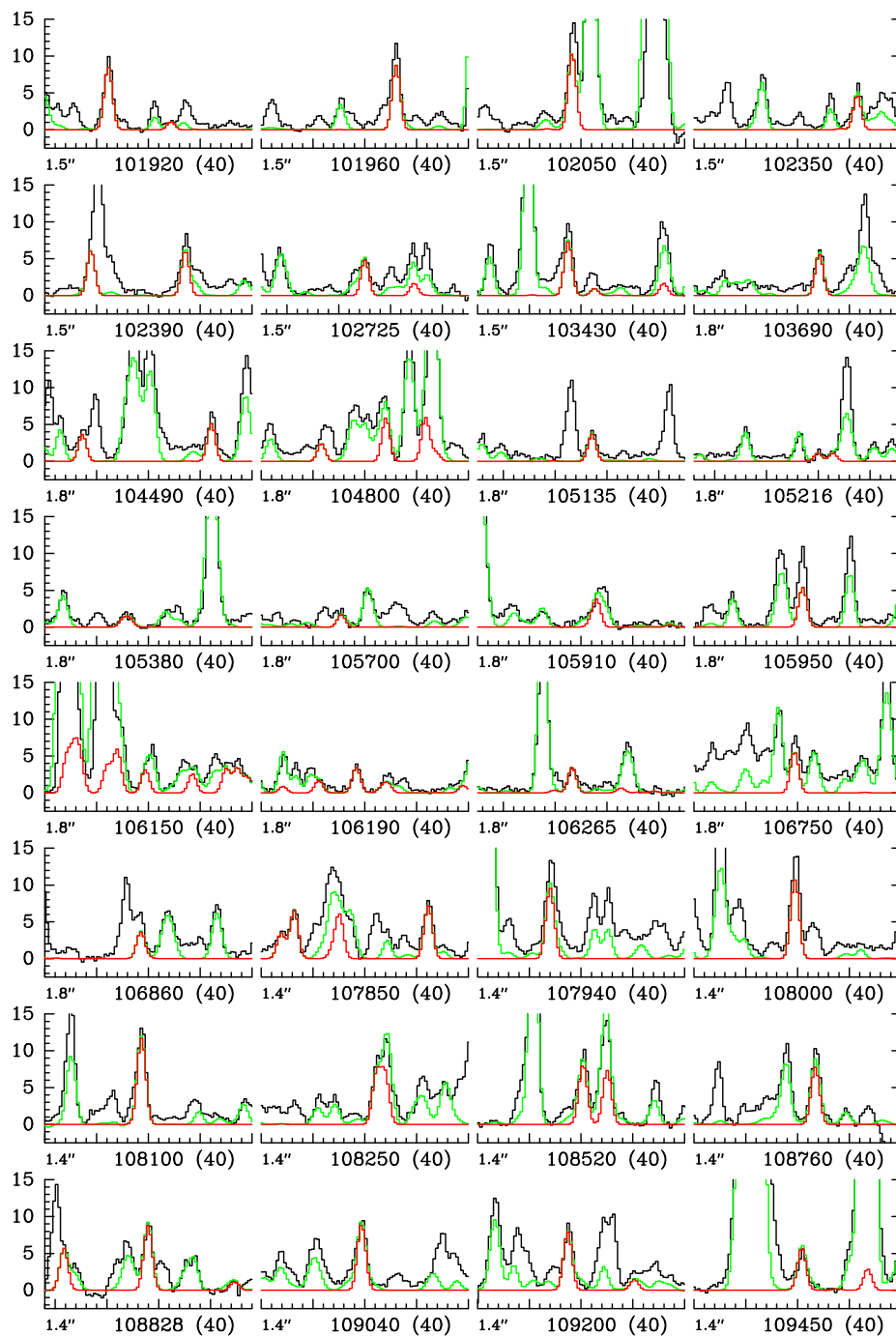


Figure S2: continued.

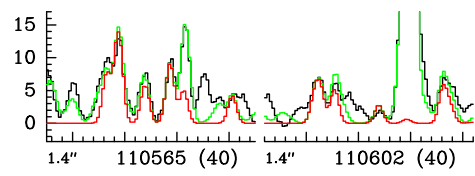


Figure S2: continued.

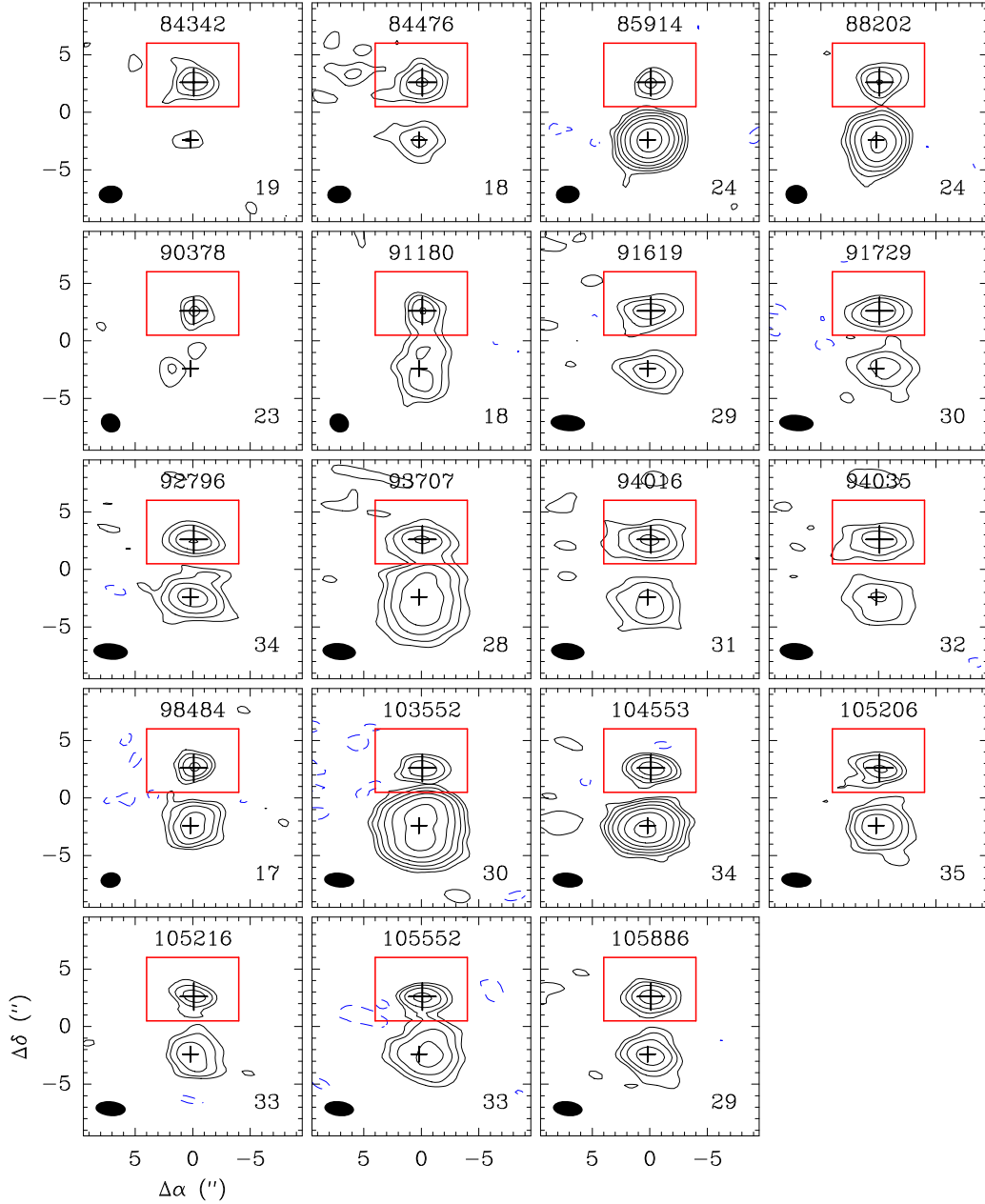


Figure S3: Integrated intensity maps of selected *i*-PrCN transitions toward the northern hot core embedded in Sgr B2(N). The central frequency of the integration range in MHz, the synthesized beam (black ellipse), and the rms noise level  $\sigma$  in  $\text{mJy beam}^{-1} \text{ km s}^{-1}$  are indicated in each panel. The negative contour (dashed blue) is  $-3\sigma$ , and the positive contours (black) are  $2^i \times 3\sigma$ , with  $i$  an integer starting at 0. The big cross indicates the position of the northern hot core. The smaller cross marks the position of the main hot core that has a lower systemic velocity, which implies that the contours outside the red box do not trace the emission of *i*-PrCN. The origin of the offsets corresponds to the phase center ( $\alpha_{J2000}=17^{\text{h}}47^{\text{m}}19.87^{\text{s}}$ ,  $\delta_{J2000}=-28^{\circ}22'16''$ ).

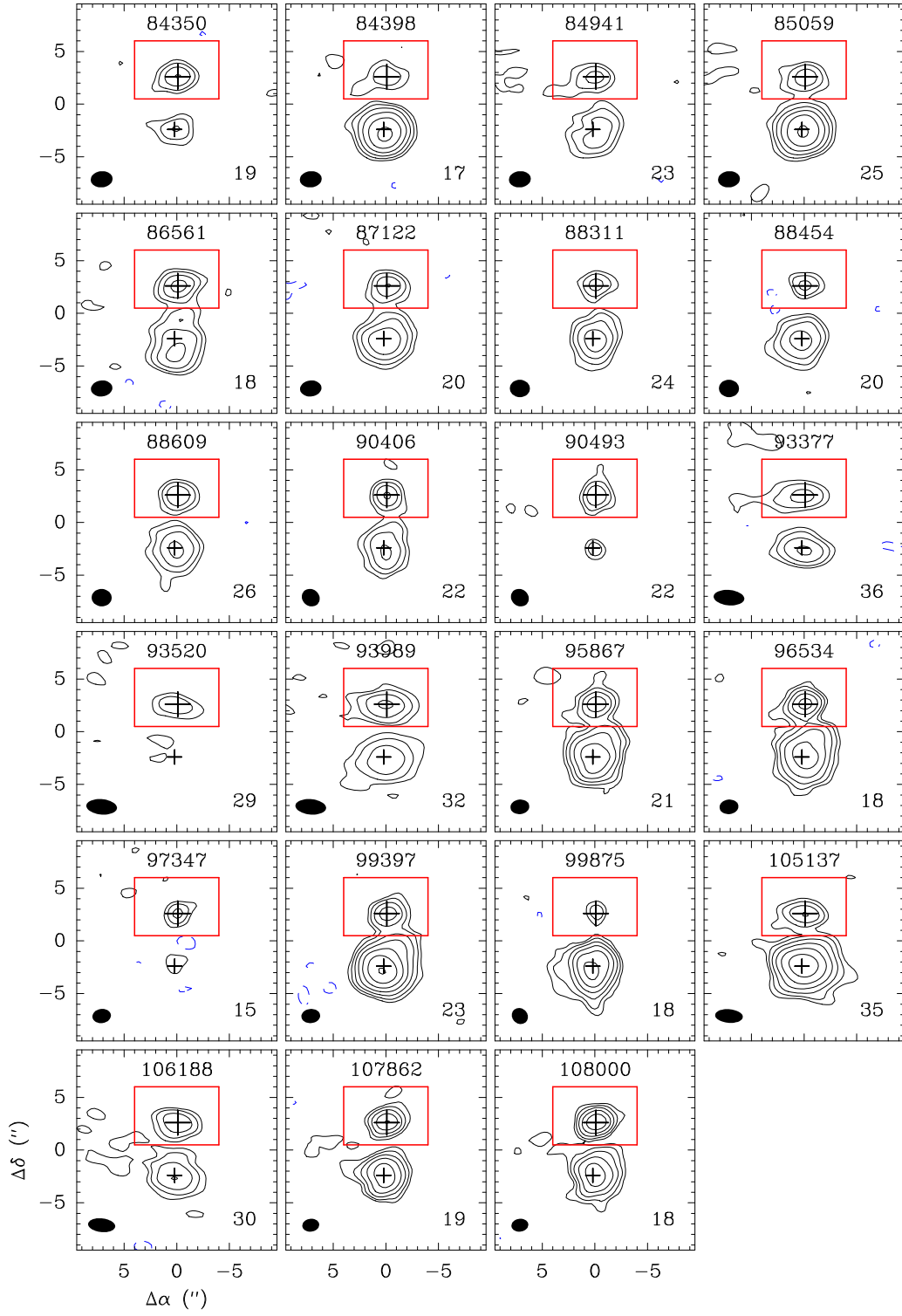


Figure S4: Integrated intensity maps of selected  $n$ -PrCN transitions toward the northern hot core embedded in Sgr B2(N). See caption of Fig. S3 for more details.

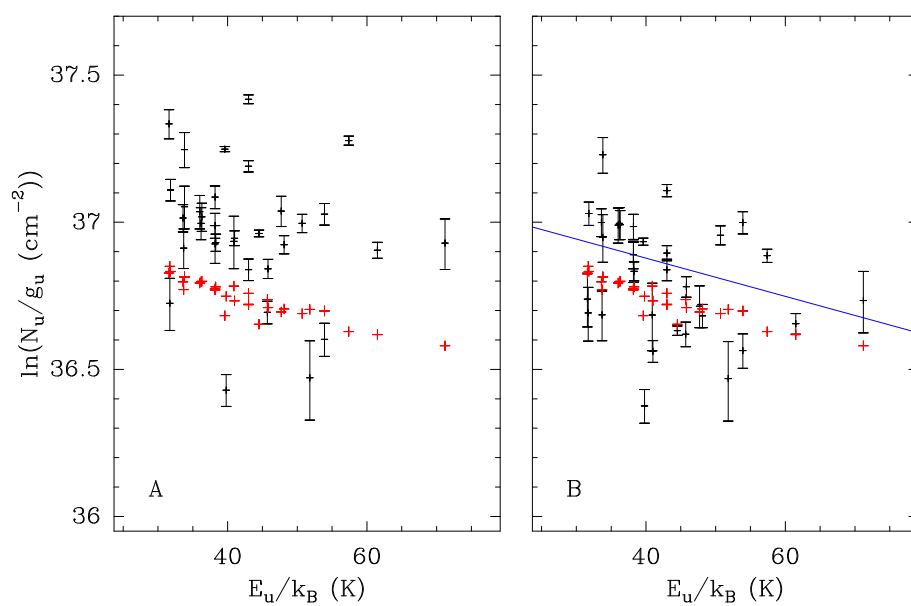


Figure S5: Population diagram of selected *i*-PrCN transitions detected toward the northern hot core embedded in Sgr B2(N). **(A)** The black crosses with error bars (SD) are derived from the observed integrated intensities while the red crosses represent the best-fit LTE model of *i*-PrCN. **(B)** Same diagram after removing the contribution of all contaminating molecules included in the full LTE model. The blue line is the result of a linear fit to the observed datapoints.

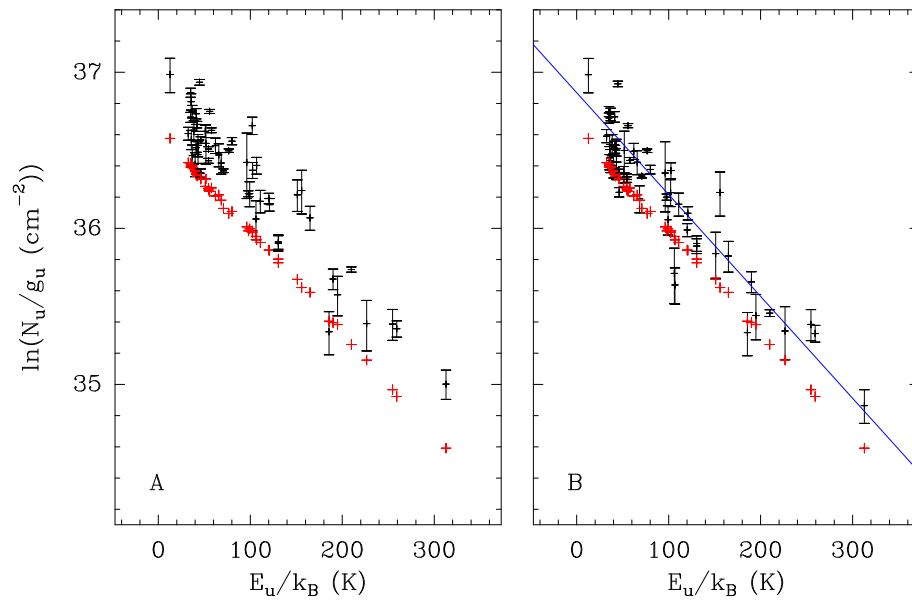


Figure S6: Population diagram of selected  $n$ -PrCN transitions detected toward the northern hot core embedded in Sgr B2(N). See caption of Fig. S5 for more details.

Table S1: Key surface/mantle reactions in the chemical model leading to the production of PrCN.

---

$\text{CH}_3 + \text{CH}_2\text{CH}_2\text{CN}$	$\rightarrow$	$n\text{-PrCN}$
$\text{C}_2\text{H}_5 + \text{CH}_2\text{CN}$	$\rightarrow$	$n\text{-PrCN}$
$\text{CH}_2\text{CH}_2\text{CH}_3 + \text{CN}$	$\rightarrow$	$n\text{-PrCN}$
$\text{CH}_3 + \text{CH}_3\text{CHCN}$	$\rightarrow$	$i\text{-PrCN}$
$\text{CH}_3\text{CHCH}_3 + \text{CN}$	$\rightarrow$	$i\text{-PrCN}$

---

Table S2: Peak fractional abundances of cyanides in the hot-core chemical models, and the associated temperatures at which those abundances are reached.

Molecule, $i$	Peak $n(i)/n(\text{H}_2)$	Temperature (K) of peak abundance
CH <sub>3</sub> CN (early)	2.4e-9	94
CH <sub>3</sub> CN (late)	2.6e-9	400
C <sub>2</sub> H <sub>3</sub> CN	2.7e-8	301
C <sub>2</sub> H <sub>5</sub> CN	1.2e-7	130
<i>i</i> -C <sub>3</sub> H <sub>7</sub> CN	8.0e-9	160
<i>n</i> -C <sub>3</sub> H <sub>7</sub> CN	3.6e-9	160